Pulsewidth-switchable ultrafast source at 114 nm

Anahita Omoumi, Michele Natile, Evangelos Papalazarou, Yoann Zaouter, Thierry Auguste, Marc Hanna, Patrick Georges, Marino Marsi

Pulsewidth-switchable ultrafast source at 114 nm

ANAHITA OMOUMI[1,2,3,*], MICHELE NATILE[3], EVANGELOS PAPALAZAROU[2], YOANN ZAOUTER[3], THIERRY AUGUSTE[4], MARC HANNA[1], PATRICK GEORGES[1], AND MARINO MARSI[2]

[1] *Université Paris-Saclay, Institut d'Optique Graduate School, CNRS, Laboratoire Charles Fabry, 91127 Palaiseau Cedex, France*
[2] *Université Paris-Saclay, Laboratoire de Physique des solides, 91400 Orsay Cedex, France*
[3] *Amplitude, 11 Avenue de Canteranne, Cité de la Photonique, 33600 Pessac, France*
[4] *Université Paris-Saclay, CEA, CNRS, Laboratoire Interactions Dynamiques et Lasers, 91191 Gif-sur-Yvette, France*
[*] *anahita.omoumi@universite-paris-saclay.fr*

Compiled August 7, 2023

Femtosecond laser sources with high repetition rate are fundamental tools enabling tabletop time-resolved and angle-resolved photoemission spectroscopy in solids. The UV and vacuum UV laser light required for the photoemission process can be generated through various frequency up-conversion techniques. We describe a VUV source at 114 nm (10.8 eV) based on an industrial grade ytterbium-doped ultrafast laser, a nonlinear pulsewidth selection stage, and two cascaded frequency tripling stages, first in crystals, second in xenon. The role of ionization in gas-based perturbative third harmonic generation phase-matching is analyzed using a simple theory, numerical simulations, and experimental data. The source features high photon flux, high repetition rate and adjustable time resolutions. Thereby, in combination with a state-of-the-art ARPES apparatus it enables the study of the electronic dynamics of the whole Brillouin zone in a large number of materials.

http://dx.doi.org/10.1364/ao.XX.XXXXXX

The rapid expansion of femtosecond laser sources with high repetition rate considerably increases the performance of a number of spectroscopy techniques, including tabletop time-resolved and angle-resolved photoemission spectroscopy (tr-ARPES) in solids. tr-ARPES is an instrumental technique in condensed matter physics which enables access to the band structure of solids as well as exploring the dynamics of quasiparticles in quantum materials [1]. The characteristics of the light source used to generate photoelectrons largely determine the performances of any tr-ARPES experiment. For instance, the achievable time and momentum/energy resolutions are related to the optical pulsewidth and bandwidth, the achievable signal to noise ratio and acquisition time are related to the repetition rate and photon flux of the source, and the accessible momentum space is determined by its central wavelength. To efficiently probe the materials, vacuum ultraviolet (VUV) or extreme-ultraviolet (EUV) ultrafast sources are required. UV light at energies around 6 eV overcomes the work function of solids and is extensively used as probe in tr-ARPES [2] but it can detect only electronic states in the proximity of the Gamma point. In order to access the whole Brillouin zone, higher energy photons are necessary.

Besides synchrotron and free-electron laser facilities, with limited access, tabletop sources based on frequency up-conversion of ultrafast lasers in the near infrared have been developed for this purpose. Depending on the up-conversion mechanism, these can be classified in two categories. First, some sources are based on non-perturbative high-harmonic generation (HHG) [3, 4], which allows access to the EUV range in a single step, often with limited photon flux and spectral resolution. Second, multiple stages of perturbative nonlinear processes can be performed to access the VUV range [5, 6], first in crystals for wavelengths above ∼200 nm, then in gases. The technology shift from titanium-doped sapphire lasers to ytterbium-based lasers has allowed an increase in repetition rate of these tabletop VUV sources and triggered renewed interest to optimize them for tr-ARPES. In particular, cascaded frequency tripling of high power laser systems at a central wavelength of ∼1 µm has been investigated [7–10]. In these sources a first stage of third-harmonic generation (THG) is performed using second-harmonic generation (SHG) and sum-frequency generation (SFG) in nonlinear crystals. This is followed by a second THG stage in a rare gas or gas mixture which is a third-order perturbative nonlinear effect subject to phase matching (PM).

Here, we describe a high repetition rate VUV source based on cascaded frequency tripling of Fourier transform-limited (FTL) pulses with a duration easily switchable between 100 fs, 500 fs, and 3 ps. The 500 fs pulses delivered by the driving ytterbium-based laser at 1030 nm and 100 kHz can be used directly or sent to a nonlinear multipass cell (MPC) that performs either spectral broadening or spectral compression, depending on the input chirp. The pulses are then sent to a first crystal-based THG stage, then focused in a xenon cell to generate the ninth harmonic.

This unique setup allows us to observe and analyze the dependence of PM pressure on experimental parameters such as pulsewidth, intensity, and focusing conditions. In particular, although THG in gases has been observed and used for decades [11], the effect of ionization on the process phase-matching has not been considered in detail, in contrast with HHG. We provide such an analysis and show that it matches the experimentally observed THG efficiency as a function of gas pressure and pulsewidth. The versatility of this source at 114 nm (10.8 eV)

in terms of spectral/temporal width, combined with a photon flux in the 10^{12} ph/s range makes it very appealing for various tr-ARPES experiments.

We first analyze the influence of ionization in the PM of perturbative gas-based THG. Early analyses of this problem [11–13] establish the possibility to obtain PM conditions by compensating neutral gas dispersion by the Gouy phase. To include analytically the effect of ionization, we turn to a description localized in one plane, similar to what is done in HHG [14, 15]. In the following, we assume that this plane corresponds to the driving pulse waist. In contrast to HHG, in the perturbative THG case, the atomic dipole phase is not relevant. Including contributions from neutral atoms, self- and cross-phase modulation (SPM, XPM) induced by the fundamental, Gouy phase, and free electrons, the phase mismatch $\Delta k = k_{3\omega} - 3k_\omega$ can be written as

$$\Delta k = \frac{\Omega}{c}\left[(n_{3\omega} - n_\omega) + (n_{2X} - n_{2S})\, I_\omega\right] + \frac{2}{z_R} + \frac{4e^2 n_e}{\Omega m_e \epsilon_0 c}, \quad \textbf{(1)}$$

where $\Omega = 3\omega$ is the angular frequency of the third harmonic, n_ω and $n_{3\omega}$ are the refractive indices at the fundamental and third harmonic wavelengths, c is the speed of light, z_R is the Rayleigh range, I_ω is the intensity of the fundamental, n_{2X} is the nonlinear index associated with XPM from the fundamental onto the third harmonic, n_{2S} is the nonlinear index governing SPM of the fundamental, e, m_e, and n_e are the electron charge, mass, and density, and ϵ_0 is the vacuum permittivity. At 343 nm, for intensities below 5×10^{13} W/cm^2 in xenon, ionization is well approximated by a three-photon process. Assuming a low ionization fraction and a Gaussian pulse profile, the electron density at the peak of the pulse is given by [16]

$$n_e = \frac{1}{4} n_0 \sigma_3 I_\omega^3 \sqrt{\frac{\pi}{3\ln 2}} \Delta t, \quad \textbf{(2)}$$

where n_0 is the initial atomic density, and Δt is the Full Width at Half Maximum (FWHM) pulsewidth. The three-photon ionization cross-section of xenon $\sigma_3 \approx 1.2 \times 10^{-39}(\mathrm{W.m^{-2}})^{-3}.\mathrm{s}^{-1}$ is found by fitting ionization rates calculated using the method described in [17] in the multiphoton regime. Substituting this expression in Eq. (1), and removing the SPM/XPM term, which is found to be negligible in our conditions (two orders of magnitude lower than the neutral atoms contribution for $I_\omega = 10^{13}$ W.cm^{-2}), the phase mismatch can be written as

$$\Delta k = \frac{\Omega}{c} p_{Xe} \Delta N_{Xe} + \frac{2}{z_R} + \kappa p_{Xe} \Delta t I^3 \quad \textbf{(3)}$$
$$\kappa = \frac{e^2 n_L \sigma_3}{\Omega m_e \epsilon_0 c} \sqrt{\frac{\pi}{3\ln 2}},$$

where n_L is the Loschmidt constant, p_{Xe} is the xenon pressure, the refractive indices have been written as $n_{\omega,3\omega} = 1 + p_{Xe} N_{\omega,3\omega}$ to bring forward their linear pressure dependence, and $\Delta N_{Xe} = N_{3\omega} - N_\omega \approx -3.7 \times 10^{-4}$ bar^{-1}. Setting $\Delta k = 0$ allows us to find a relationship between the PM pressure and the intensity

$$I_\omega^3 = -\frac{1}{\kappa \Delta t}\left(\frac{\Omega}{c}\Delta N_{Xe} + \frac{2}{z_R p_{Xe}}\right). \quad \textbf{(4)}$$

The first term in the parenthesis, corresponding to the neutral dispersion, is negative, while the second one, corresponding to the Gouy phase, is positive. Figure 1 illustrates this relationship at a driving wavelength of 343 nm in xenon for three focusing conditions and pulse durations. When ionization is negligible ($I \to 0$), we recover the balance between neutral dispersion and Gouy phase, defining a first horizontal asymptote.

$$z_R p_{Xe} = -2\frac{c}{\Omega \Delta N_{Xe}}. \quad \textbf{(5)}$$

As the intensity increases, the PM pressure increases because the neutral atoms dispersion must compensate for the ionization contribution. At high intensity the neutral atoms dispersion contribution must be much higher than the Gouy phase contribution to balance ionization, leading to a second vertical asymptote

$$I_\omega^3 = -\frac{1}{\kappa \Delta t}\frac{\Omega}{c}\Delta N_{Xe}. \quad \textbf{(6)}$$

The horizontal asymptote moves up to a higher pressure when the waist radius is decreased, and the vertical asymptote is shifted to a higher intensity when reducing the pulse duration. As in the case of HHG [15], shorter pulsewidths allow the possibility of phase-matching over a larger intensity range, because the peak intensity can be reached for a lower ionization fraction.

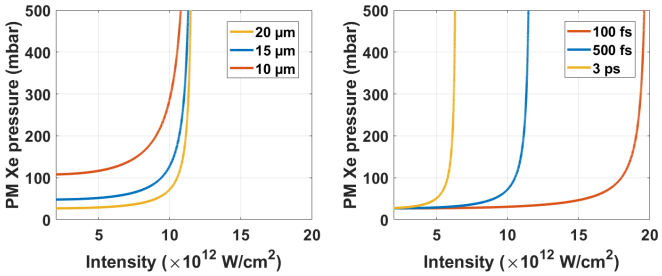

Fig. 1. PM pressure as a function of intensity of the driving pulse at 343 nm in the Xe cell. Left: different waist radii at fixed 500 fs pulse duration. Right: different pulse durations at fixed waist radius of 10 µm.

To capture physical effects beyond this simplified analysis, that considers phase-matching in a single plane at maximum intensity in space and time, we compare the experimental results with numerical simulations. These simulations are based on solving two coupled envelope equations for the fundamental and THG fields in (2+1)D geometry (r, z, t), assuming radial symmetry. They take into account diffraction, dispersion through a Sellmeier equation for xenon [13], THG, SPM, XPM, assuming a single $\chi^{(3)}$ value corresponding to a nonlinear index $n_2 = 5.2 \times 10^{-23}\mathrm{m}^2/\mathrm{W}$ for all these processes, and ionization-related effects including free electron dispersion. This model allows to get a more accurate picture, taking into account the temporal, transverse and longitudinal spatial variations in intensity and phase for both beams. For comparison with experiments, the only slightly adjusted parameter is the waist radius, because it was difficult to estimate its precise value due to the limited resolution of the camera used.

We now turn to the description of the experimental setup, shown in Fig. 2. It starts with an Yb-doped industrial laser source (Tangor, Amplitude) that delivers 500 fs 300 µJ pulses at 100 kHz repetition rate and 1030 nm wavelength. This laser is delivered with a remote-controlled grating-based compressor unit that allows easy chirp adjustment of the output pulses. Using a set of flip mirrors, the pulses can either be sent directly to the crystal-based frequency tripling stage to seed the 500 fs beamline, or to a MPC to manipulate the pulse duration. This MPC is

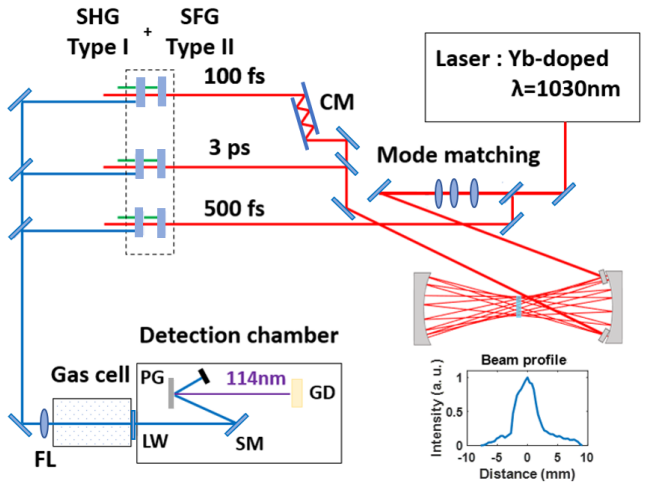

Fig. 2. GD: gold detector, SM: spherical mirror, PG: plane grating, LW: LiF window, FL: focusing lens, CM: chirped mirrors. Layout of the experimental setup. Inset: beam profile of the 114 nm pulses based on a knife edge measurement after the grating.

designed so that, if the input pulses are FTL, it compresses them down to 100 fs [18, 19], while if they are negatively stretched to 3 ps, it compresses the spectrum down to the FTL limit [20]. Indeed, applying self-phase modulation on negatively chirped pulses results in instantaneous frequency shifts that suppress the edges of the input spectrum. This results in a very easy switch between 100 fs (temporal compression), 500 fs (initial laser source), and 3 ps (spectral compression) FTL pulses.

The MPC is composed of two concave mirrors with a radius of curvature of 300 mm separated by 550 mm in a Herriott configuration [21] inside which a 5 mm-thick AR-coated fused silica plate is inserted to provide nonlinearity [18]. An arrangement of three lenses is used to match the input beam to the stationary beam of the MPC, and the pulses are propagating through 15 roundtrips before being sent out. At the output of the MPC, another flip mirror is used to send the pulses to a set of chirped mirrors introducing a total group-delay dispersion of -16000 fs^2 (spectrally broadened pulses) or directly to the frequency tripling stage (spectrally compressed pulses). The spectral and temporal profiles of each beamline are shown in Fig. 3. The time-bandwidth products are 0.51, 0.43, and 0.5 for the 100 fs, 500 fs, and 3 ps pulses respectively.

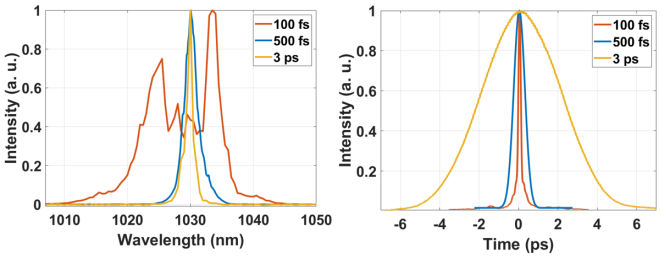

Fig. 3. Left: measured spectra at 1030 nm. Right: measured autocorrelation traces at 1030 nm.

The nonlinear crystals used in the first THG stage (all provided by Crylight) must be adapted to the three different pulse durations. Each beamline of 100 fs, 500 fs and 3 ps with energies of 150 µJ, 300 µJ and 200 µJ respectively, is therefore sent to three parallel tripling stages. Each stage is based on SHG in a first BBO crystal (thicknesses of 0.5, 1, and 2 mm for 100 fs, 500 fs and 3 ps respectively), followed by SFG in a second BBO crystal (thicknesses of 0.75, 1.5, and 2 mm for 100 fs, 500 fs and 3 ps respectively). Before the second, gas-based THG stage, the available energies at 343 nm are 15 µJ, 30 µJ, and 30 µJ for driving pulse durations of 100 fs, 500 fs, and 3 ps respectively. The lower pulse energy available at 100 fs duration is due to the losses of the chirped mirrors, and lower tripling efficiency. Although the pulse durations at 343 nm are not measured directly, the measured spectra indicate that the pulse durations at 1030 nm are approximately conserved at 343 nm.

The second THG stage consists of a xenon-filled cell in which the beam at 343 nm is focused, yielding a beam at 114 nm. Both beams enter the under-vacuum detection chamber transmitted through a lithium fluoride (LiF) window. The photon flux is estimated by measuring the drain current from the surface of a gold target [22] inserted just after the LiF window. Because the work funtion of gold is 5.2 eV while the photon energies of the 343 nm and 114 nm light are 3.6 eV and 10.8 eV respectively, the detection of stray light is efficiently suppressed. We have also experimentally verified that illuminating the gold surface with the full power at 343 nm in the absence of THG (gas cell under vacuum), in the three different pulse duration cases, resulted in negligible measured current. A knife edge measurement of the 114 nm beam profile, performed after a spherical mirror and a dispersive grating to filter out the 343 nm beam, is reported in the inset in Fig. 2.

We start by investigating PM effects at a driving pulse duration of 500 fs. Figure 4 shows the experimentally measured and simulated power of the 114 nm beam as a function of gas pressure, for different focused beam sizes and energies. As observed in Fig. 4 (right), the PM pressure increases for smaller focused beam diameter, as expected for example from Eq. (5). Fig. 4 (left) shows that the PM gas pressure also increases for increasing input energy, as predicted by Eq. (4), because of the onset of the ionization, causing a non-negligible contribution of free electrons. Numerical simulations are in quantitative agreement, reproducing both the PM pressure shifts and changes in the curve shapes. In Fig. 5, the measured power at 114 nm as a function of Xe pressure for pulse durations of 100 fs and 3

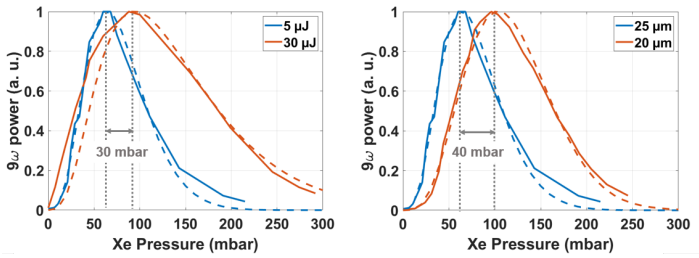

Fig. 4. Measured (solid line) and simulated (dashed line) power at 114 nm as a function of Xe pressure, normalized to the maximum value. Left: the beam diameter is 25 µm (obtained using a lens with a focal length of 200 mm), the pulse energies are 5 µJ (blue) and 30 µJ (red). Right: the input energy is 5 µJ, the focused beam diameters are 20 µm (red) and 25 µm (blue), achieved using lenses with focal lengths of 150 mm and 200 mm, respectively.

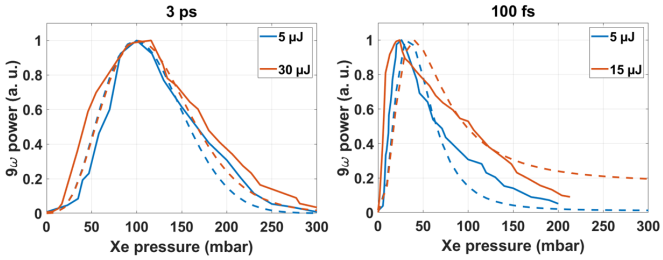

Fig. 5. Measured (solid line) and simulated (dashed line) power at 114 nm as a function of Xe pressure. Left: the pulse duration is 3 ps, the pulse energies are 5 µJ and 30 µJ. Right: the pulse duration is 100 fs, the pulse energies are 5 µJ and 15 µJ.

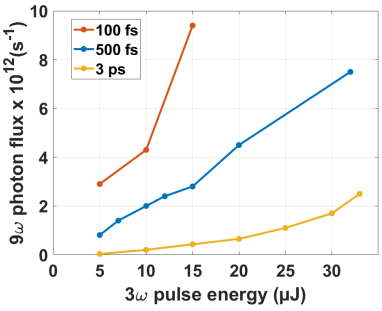

Fig. 6. Estimated photon flux at 114 nm as a function of input power at 343 nm for each pulse duration.

ps are presented. The focused spot diameter is 38 µm for the 100 fs pulses and 22 µm for the 3 ps pulses, which explains the difference in PM pressure at low pulse energies. In contrast to the data obtained for 500 fs pulses, we do not observe a PM pressure shift as a function of input pulse energy. In both cases, this can be explained by the fact that the available energies and focusing conditions lead to intensities that are below the onset of significant ionization. As discussed above, this intensity threshold is much higher for 100 fs pulses than for 3 ps pulses. The simulations are in reasonable agreement with the observed data.

We now comment on the absolute photon fluxes at 114 nm measured for the three pulse durations. To estimate them, the detected current is converted to photon flux assuming a photoelectric yield for Au of 0.08 electron per photon [22]. Figure 6 shows the photon flux as a function of input pulse energy when the pressure is fixed to the PM pressure for the maximum energy available for each beamline. At a given pulse energy, the intensity is higher for the 100 fs beamline, which translates into a higher efficiency. It is also apparent that the conversion efficiency increases with power for the 100 fs and 3 ps cases, for which ionization effects are small, which is expected for an unsaturated phase-matched third order process. However, for the 500 fs case, this efficiency appears to be almost constant. This could be caused by the fact that ionization effects are local in space and time, resulting in a constant average efficiency as the power is increased. The maximum measured photon fluxes after the LiF window at 100 fs, 500 fs, and 3 ps are 9×10^{12}, 7×10^{12}, and 2×10^{12} ph/s respectively. Taking into account the transmission efficiency of the LiF window which is measured to be 30%, these photon fluxes correspond to optical-to-optical power internal conversion efficiencies of 3×10^{-5}, 1×10^{-5}, and 3×10^{-6}.

In conclusion, we report a VUV table-top source at 114 nm based on cascaded THG of FTL driving pulses at 1030 nm with switchable pulse durations of 100 fs, 500 fs, and 3 ps. Assuming that the spectral widths are maintained during the wavelength conversion stages, as indicated by numerical simulations, this corresponds to energy resolutions of 15, 3, and 0.5 meV. This versatility in terms of temporal and spectral resolution, combined with a high repetition rate and sufficient photon flux should make this type of source very appealing for future tr-ARPES setups in particular in combination with high-luminosity spectrometers [23].

Funding. Agence Nationale de la Recherche (ANR-21-CE30-0038-SHOTIME).

Acknowledgment. The authors acknowledge helpful discussions with Z. Zhao, F. Cilento and O. Tjernberg.

Disclosures. The authors declare no conflicts of interest.

Data Availability Statement. Data underlying the results presented in this article are not publicly available at this time but may be obtained from the authors upon reasonable request.

REFERENCES

1. J. A. Sobota, Y. He, and Z.-X. Shen, Rev. Mod. Phys. **93**, 025006 (2021).
2. J. Faure, J. Mauchain, E. Papalazarou, W. Yan, J. Pinon, M. Marsi, and L. Perfetti, Rev. Sci. Instruments **83**, 043109 (2012).
3. J. Wang, F. Chen, M. Pan, S. Xu, R. Lv, J. Liu, Y. Li, S. Fang, Y. Chen, J. Zhu, D. Zhang, T. Qian, C. Yun, K. Zhao, H. Ding, and Z. Wei, Opt. Express **31**, 9854 (2023).
4. Q. Guo, M. Dendzik, A. Grubišić-Čabo, M. H. Berntsen, C. Li, W. Chen, B. Matta, U. Starke, B. Hessmo, J. Weissenrieder, and O. Tjernberg, Struct. Dyn. **9** (2022). 024304.
5. R. Forbes, P. Hockett, and R. Lausten, Opt. Lett. **47**, 2410 (2022).
6. Y. He, I. M. Vishik, M. Yi, S. Yang, Z. Liu, J. J. Lee, S. Chen, S. N. Rebec, D. Leuenberger, A. Zong *et al.*, Rev. Sci. Instruments **87**, 011301 (2016).
7. M. H. Berntsen, O. Götberg, and O. Tjernberg, Rev. Sci. Instruments **82**, 095113 (2011).
8. Z. Zhao and Y. Kobayashi, Opt. Express **25**, 13517 (2017).
9. X. Zhou, S. He, G. Liu, L. Zhao, L. Yu, and W. Zhang, Reports on Prog. Phys. **81**, 062101 (2018).
10. S. Peli, D. Puntel, D. Kopic, B. Sockol, F. Parmigiani, and F. Cilento, J. Electron Spectrosc. Relat. Phenom. **243**, 146978 (2020).
11. J. Ward and G. New, Phys. Rev. **185**, 57 (1969).
12. G. Bjorklund, IEEE J. Quantum Electron. **11**, 287 (1975).
13. R. Mahon, T. McIlrath, V. Myerscough, and D. Koopman, IEEE J. Quantum Electron. **15**, 444 (1979).
14. S. Kazamias, S. Daboussi, O. Guilbaud, K. Cassou, D. Ros, B. Cros, and G. Maynard, Phys. Rev. A **83**, 063405 (2011).
15. S. Hädrich, J. Rothhardt, M. Krebs, S. Demmler, A. Klenke, A. Tünnermann, and J. Limpert, J. Phys. B: At. Mol. Opt. Phys. **49**, 172002 (2016).
16. J. Schwarz, P. Rambo, and J. Diels, Appl. Phys. B **72**, 343 (2001).
17. A. Perelomov, V. Popov, and M. Terentev, JETP **23**, 924 (1966).
18. J. Schulte, T. Sartorius, J. Weitenberg, A. Vernaleken, and P. Russbueldt, Opt. Lett. **41**, 4511 (2016).
19. L. Lavenu, M. Natile, F. Guichard, X. Délen, M. Hanna, Y. Zaouter, and P. Georges, Opt. express **27**, 1958 (2019).
20. N. Daher, F. Guichard, X. Délen, Y. Zaouter, M. Hanna, and P. Georges, Opt. Express **28**, 21571 (2020).
21. D. Herriott, H. Kogelnik, and R. Kompfner, Appl. Opt. **3**, 523 (1964).
22. B. Feuerbacher and B. Fitton, J. Appl. Phys. **43**, 1563 (1972).
23. J. Zhang, Z. Chen, E. Papalazarou, M. Marsi, A. Omoumi, and J. Caillaux, "Spin and orbital texture of quantum materials from dichroism in

the ultrafast photoemission yield," in *Advances in Ultrafast Condensed Phase Physics III,* , vol. 12132 (SPIE, 2022), pp. 33–38.

FULL REFERENCES

1. J. A. Sobota, Y. He, and Z.-X. Shen, "Angle-resolved photoemission studies of quantum materials," Rev. Mod. Phys. **93**, 025006 (2021).
2. J. Faure, J. Mauchain, E. Papalazarou, W. Yan, J. Pinon, M. Marsi, and L. Perfetti, "Full characterization and optimization of a femtosecond ultraviolet laser source for time and angle-resolved photoemission on solid surfaces," Rev. Sci. Instruments **83**, 043109 (2012).
3. J. Wang, F. Chen, M. Pan, S. Xu, R. Lv, J. Liu, Y. Li, S. Fang, Y. Chen, J. Zhu, D. Zhang, T. Qian, C. Yun, K. Zhao, H. Ding, and Z. Wei, "High-flux wavelength tunable xuv source in the 12–40.8 ev photon energy range with adjustable energy and time resolution for tr-arpes applications," Opt. Express **31**, 9854–9871 (2023).
4. Q. Guo, M. Dendzik, A. Grubišić-Čabo, M. H. Berntsen, C. Li, W. Chen, B. Matta, U. Starke, B. Hessmo, J. Weissenrieder, and O. Tjernberg, "A narrow bandwidth extreme ultra-violet light source for time- and angle-resolved photoemission spectroscopy," Struct. Dyn. **9** (2022). 024304.
5. R. Forbes, P. Hockett, and R. Lausten, "Efficient generation of the 7th harmonic of ti:sapphire (114.6 nm) vacuum ultraviolet pulses with 60 fs duration by non-collinear four-wave mixing in argon," Opt. Lett. **47**, 2410–2413 (2022).
6. Y. He, I. M. Vishik, M. Yi, S. Yang, Z. Liu, J. J. Lee, S. Chen, S. N. Rebec, D. Leuenberger, A. Zong *et al*., "Invited article: High resolution angle resolved photoemission with tabletop 11 ev laser," Rev. Sci. Instruments **87**, 011301 (2016).
7. M. H. Berntsen, O. Götberg, and O. Tjernberg, "An experimental setup for high resolution 10.5 ev laser-based angle-resolved photoelectron spectroscopy using a time-of-flight electron analyzer," Rev. Sci. Instruments **82**, 095113 (2011).
8. Z. Zhao and Y. Kobayashi, "Realization of a mw-level 10.7-ev (λ= 115.6 nm) laser by cascaded third harmonic generation of a yb: fiber cpa laser at 1-mhz," Opt. Express **25**, 13517–13526 (2017).
9. X. Zhou, S. He, G. Liu, L. Zhao, L. Yu, and W. Zhang, "New developments in laser-based photoemission spectroscopy and its scientific applications: a key issues review," Reports on Prog. Phys. **81**, 062101 (2018).
10. S. Peli, D. Puntel, D. Kopic, B. Sockol, F. Parmigiani, and F. Cilento, "Time-resolved vuv arpes at 10.8 ev photon energy and mhz repetition rate," J. Electron Spectrosc. Relat. Phenom. **243**, 146978 (2020).
11. J. Ward and G. New, "Optical third harmonic generation in gases by a focused laser beam," Phys. Rev. **185**, 57 (1969).
12. G. Bjorklund, "Effects of focusing on third-order nonlinear processes in isotropic media," IEEE J. Quantum Electron. **11**, 287–296 (1975).
13. R. Mahon, T. McIlrath, V. Myerscough, and D. Koopman, "Third-harmonic generation in argon, krypton, and xenon: bandwidth limitations in the vicinity of lyman-α," IEEE J. Quantum Electron. **15**, 444–451 (1979).
14. S. Kazamias, S. Daboussi, O. Guilbaud, K. Cassou, D. Ros, B. Cros, and G. Maynard, "Pressure-induced phase matching in high-order harmonic generation," Phys. Rev. A **83**, 063405 (2011).
15. S. Hädrich, J. Rothhardt, M. Krebs, S. Demmler, A. Klenke, A. Tünnermann, and J. Limpert, "Single-pass high harmonic generation at high repetition rate and photon flux," J. Phys. B: At. Mol. Opt. Phys. **49**, 172002 (2016).
16. J. Schwarz, P. Rambo, and J. Diels, "Measurements of multiphoton ionization coefficients with ultrashort ultraviolet laser pulses," Appl. Phys. B **72**, 343–347 (2001).
17. A. Perelomov, V. Popov, and M. Terentev, "Ionization of atoms in an alternating electric field," JETP **23**, 924–934 (1966).
18. J. Schulte, T. Sartorius, J. Weitenberg, A. Vernaleken, and P. Russbueldt, "Nonlinear pulse compression in a multi-pass cell," Opt. Lett. **41**, 4511–4514 (2016).
19. L. Lavenu, M. Natile, F. Guichard, X. Délen, M. Hanna, Y. Zaouter, and P. Georges, "High-power two-cycle ultrafast source based on hybrid nonlinear compression," Opt. express **27**, 1958–1967 (2019).
20. N. Daher, F. Guichard, X. Délen, Y. Zaouter, M. Hanna, and P. Georges, "Spectral compression in a multipass cell," Opt. Express **28**, 21571–21577 (2020).
21. D. Herriott, H. Kogelnik, and R. Kompfner, "Off-axis paths in spherical mirror interferometers," Appl. Opt. **3**, 523–526 (1964).
22. B. Feuerbacher and B. Fitton, "Experimental investigation of photoemission from satellite surface materials," J. Appl. Phys. **43**, 1563–1572 (1972).
23. J. Zhang, Z. Chen, E. Papalazarou, M. Marsi, A. Omoumi, and J. Caillaux, "Spin and orbital texture of quantum materials from dichroism in the ultrafast photoemission yield," in *Advances in Ultrafast Condensed Phase Physics III,* vol. 12132 (SPIE, 2022), pp. 33–38.